ACS APPLIED MATERIALS & INTERFACES

www.acsami.org

Research Article

Unraveling Thermal Transport Properties of $MoTe_2$ Thin Films Using the Optothermal Raman Technique

Carlos Rodriguez-Fernandez,* Arttu Nieminen, Faisal Ahmed, Jesse Pietila, Harri Lipsanen, and Humeyra Caglayan*

Cite This: *ACS Appl. Mater. Interfaces* 2023, 15, 35692−35700

Read Online

ACCESS | Metrics & More | Article Recommendations | Supporting Information

ABSTRACT: Understanding phonon transport and thermal conductivity of layered materials is not only critical for thermal management and thermoelectric energy conversion but also essential for developing future optoelectronic devices. Optothermal Raman characterization has been a key method to identify the properties of layered materials, especially transition-metal dichalcogenides. This work investigates the thermal properties of suspended and supported $MoTe_2$ thin films using the optothermal Raman technique. We also report the investigation of the interfacial thermal conductance between the $MoTe_2$ crystal and the silicon substrate. To extract the thermal conductivity of the samples, temperature- and power-dependent measurements of the in-plane E^1_{2g} and out-of-plane A_{1g} optical phonon modes were performed. The results show remarkably low in-plane thermal conductivities at room temperature, at around 5.16 ± 0.24 W/m·K and 3.72 ± 0.26 W/m·K for the E^1_{2g} and the A_{1g} modes, respectively, for the 17 nm thick sample. These results provide valuable input for the design of electronic and thermal $MoTe_2$-based devices where thermal management is vital.

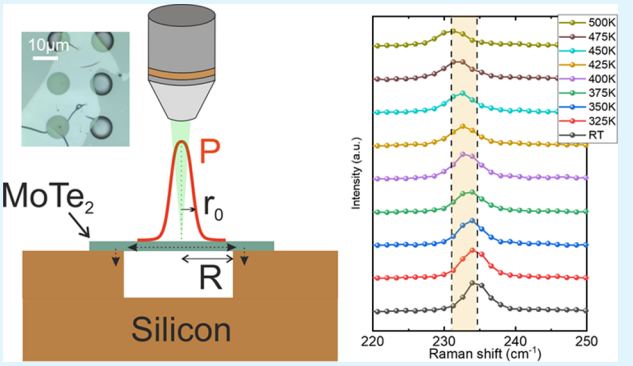

KEYWORDS: *optothermal characterization, $MoTe_2$, Raman spectroscopy, TMDs, thermal conductivity, and interfacial thermal conductance.*

INTRODUCTION

Transition-metal dichalcogenides (TMDs) have been extensively studied as potential materials for the next generation of optoelectronic devices because of their unique and tunable physical and chemical properties at nanometric scale, including thickness-dependent band gaps, strain engineering, high carrier mobility, broadband optical absorption, high optical response, etc.[1−7] These layered materials exhibit strong covalent bonds in-plane and weak out-of-plane van der Waals forces that enable the preparation of uniform atomic layers by mechanical or chemical exfoliation. Moreover, these materials have good mechanical strength[8] and nanoscale dimensionality, resulting in huge potential for electronic applications, energy, storage, biomedicine, catalysis, etc.[9−11] Besides these applications, mono- and few-layer TMD materials have been considered forthcoming candidates for thermoelectric (TE) and energy-efficient device applications.[12,13] The conversion efficiency to transform waste heat into electrical power of a TE material is defined by the dimensionless figure of merit ZT which is directly proportional to the square of the Seebeck coefficient and inversely proportional to the thermal conductivity.[14] The dichalcogenides of group VI, 2H-MX_2 (M = Mo, W; X = S, Se, Te) are promising materials for these applications, owing to their phonon properties, relatively low thermal conductivity, and high Seebeck coefficient.[15−17]

Among the widely studied TMDs, the compound $MoTe_2$ has been in the spotlight for its polymorphic nature at room temperature with an extremely small energy difference (40 meV) between the semiconducting 2H phase (α-phase) and the metastable semi-metallic 1T′ phase (β-phase).[18−20] In addition, $MoTe_2$ is the only material among group VI that can be grown in both α- (2H) and β-(1T′) phases, and their phase change has been reported by strain,[21] joule heating,[22] ionic liquid gating,[23] electrostatic doping,[24] and laser irradiation.[18] This makes $MoTe_2$ an excellent candidate for the fabrication of two-dimensional (2D) hetero-phase homojunction and opens new possibilities for designing low-cost applications in utilizing the phase-engineering of $MoTe_2$. Nevertheless, as reported earlier, the characteristics of $MoTe_2$ are greatly influenced by external perturbations such as thermal stress compared with

Received: April 28, 2023
Accepted: June 29, 2023
Published: July 12, 2023

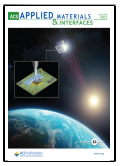

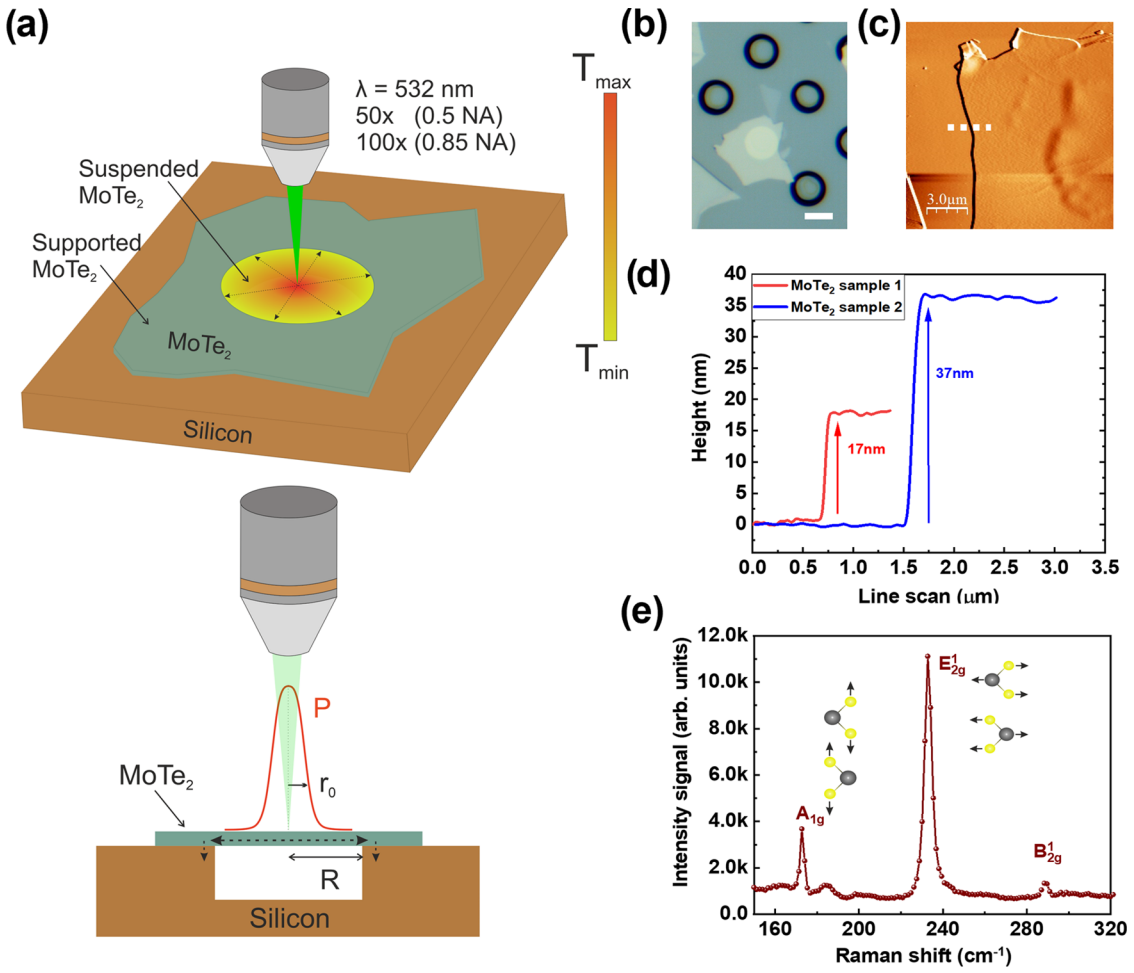

Figure 1. (a) Sketch of optothermal Raman experiment for the $MoTe_2$ samples placed on the Si substrate. (b) Optical microscope image of $MoTe_2$ sample transferred over the prefabricated holes. (c) AFM example of a 37 nm thick sample and (d) step height of the exfoliated $MoTe_2$ samples after being transferred to the Si substrate. (e) Room-temperature Raman spectrum of supported $MoTe_2$ (sample 1, 17 nm flake) with the schematic representation of the E^1_{2g} and A_{1g} modes.

other counterpart materials.[25] The influence of thermal stress is directly proportional to the heat capacity and thermal conductivity of a certain material. This combined with the readily phase change of $MoTe_2$ by localized heating may generate Te migration during the operation of $MoTe_2$-based memory devices[26] or heat-induced structural phase transition of the 2D $MoTe_2$ film under Joule heating.[27] Understanding phonon properties would enable the extraction of the thermal coefficient and thermal conductivity, which is of fundamental importance for such device applications. The thermal transport properties of $MoTe_2$ have only been investigated theoretically via computational methods[28,29] which revealed $MoTe_2$ as a promising candidate for thermoelectric applications. Although these studies provide a basic understanding of thermal transport in monolayer 2H-$MoTe_2$ for future applications, the thermal transport properties have not been experimentally analyzed.

The noncontact optothermal Raman technique has been considered one of the most robust methods for measuring the thermal properties and thermal conductivity of a wide range of 2D materials.[30−38] In addition, this technique is not limited to atomically thin layers and has also been extended to relatively thick layers with adequate laser power intensity to cause the local heating of the sample.[39,40] In this work, we present the temperature- and power-absorbed- dependent analysis of thin $MoTe_2$ films that permit the extraction and calculation of the interfacial thermal conductance with the substrate and the thermal conductivity of the material. The obtained room-temperature thermal conductivity for $MoTe_2$ flake is remarkably low compared with other TMD materials characterized by the optothermal Raman method. These results provide valuable information about the understanding of the heat conduction of $MoTe_2$ and should be considered in the fabrication of polymorphic engineering of $MoTe_2$ for thermoelectric and optoelectronic applications.

RESULTS AND DISCUSSION

Prior to the detailed optothermal analysis, multilayered $MoTe_2$ flakes were mechanically exfoliated from commercially purchased $MoTe_2$ crystal using Scotch tape and transferred onto clean Si substrates with prefabricated holes. The Si substrate presents a higher thermal conductivity (around 150 W/m·K)[41] that can act as a heat sink. This enables the direct comparison of the temperature and power coefficients between the suspended and the supported characterized samples. The schematic of the optothermal Raman technique employed in the characterization of $MoTe_2$ flakes suspended over circular holes on the Si substrate can be observed in Figure 1a. This technique requires a two-step procedure. First, the temperature

https://doi.org/10.1021/acsami.3c06134
ACS Appl. Mater. Interfaces 2023, 15, 35692−35700

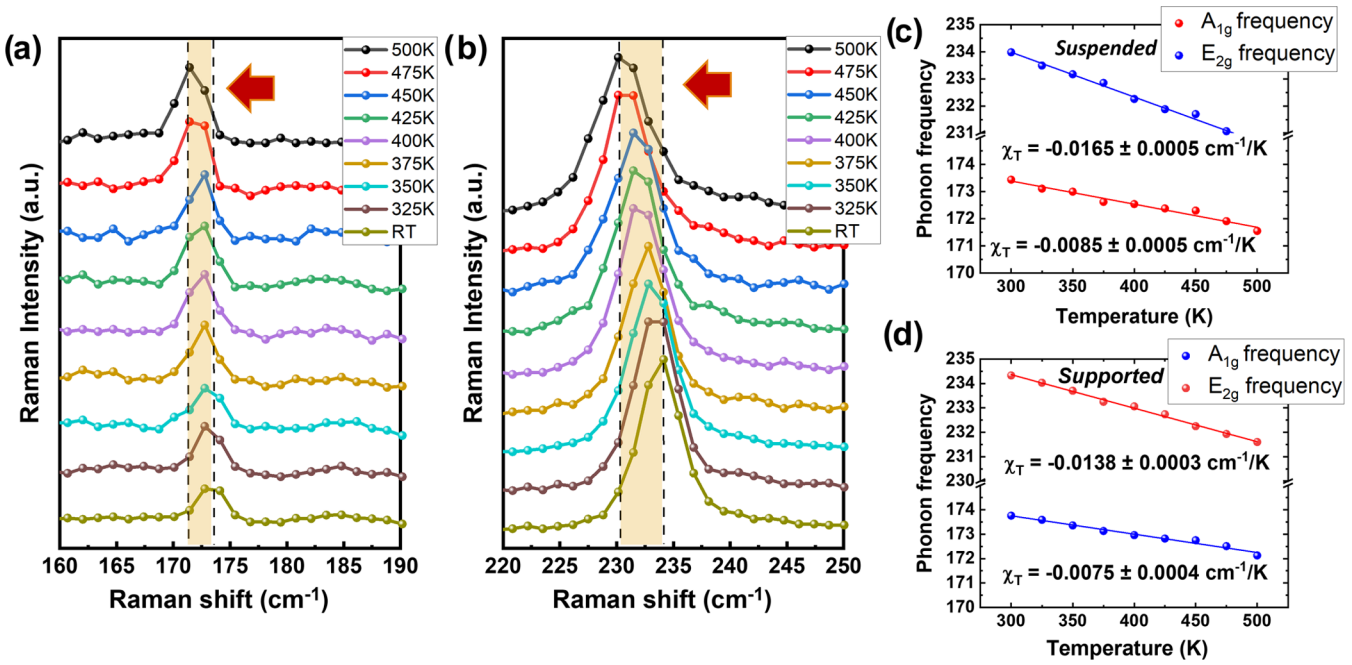

Figure 2. (a) Temperature-dependent Raman spectra of (a) A_{1g} and (b) E^1_{2g} for suspended $MoTe_2$ (sample 1, 17 nm) with a temperature range from room temperature (around 293 K) to 500 K. Temperature-dependent coefficients of the characterized E^1_{2g} (blue circles) and A_{1g} (red circles) phonon modes for the (c) suspended and (d) supported $MoTe_2$. These points have been individually extracted from the Lorentzian fit of the Raman peaks.

dependence of the position of the optical phonon modes of the $MoTe_2$ flakes is studied to extract the first-order temperature coefficient (χ_T), which acts as a Raman thermometer. After that, the laser-power-dependent Raman spectra of the selected phonon modes are recorded to determine the amount of absorbed power on either the supported or the suspended $MoTe_2$ at room temperature. The 100× and 50× objectives with different numerical apertures were employed to perform the power-dependent measurements. Having the local temperature raised by the laser power, the heat diffusion equations can be solved. The cross section of the $MoTe_2$ on the Si substrate is also displayed in Figure 1a, where holes with a diameter of 10 μm were fabricated by maskless lithography (see the Methods Section). The microscope image in Figure 1b presents a thin $MoTe_2$ flake that covers holes on the Si substrate. The multilayer $MoTe_2$ samples with a thickness in the range of 15−40 nm are preferred in our experiments due to the fact that multilayer samples are environmentally robust, exhibit band gap close to Silicon, and can be transformed from semiconducting to the metallic phase with laser. Importantly, we use two samples with similar thicknesses, noted as sample 1 (17 nm thick) and sample 2 (37 nm thick), in order to monitor the reproducibility of the employed method for the determination of thermal conductivity. The height profile measured by atomic force microscope (AFM) across the edge of the flakes is displayed in Figure 1d for both samples. To corroborate the quality of the transferred sample over the holes, the samples were characterized by micro-Raman spectroscopy at room temperature and low power intensity, as presented in Figure 1e.

As the point group of semiconducting bulk 2H-$MoTe_2$ belongs to D_{6h} symmetry, the unit cell is composed of six atoms, resulting in 18 phonon modes (15 of them are optical modes). Due to the center of inversion, bulk 2H-$MoTe_2$ can be split into gerade (marked with subindex g) and ungerade (subindex u) modes. The gerade modes present a change in the polarizability but do not have a dipole moment, and they are Raman-active modes. Ungerade modes have a dipole moment and, therefore, these modes are infrared active. Since bulk 2H-$MoTe_2$ is a center-symmetric crystal, the Raman modes cannot appear in an infrared spectrum and vice versa, they are exclusive. Thus, the irreducible representation of the lattice vibration at Γ point of the Brillouin zone (zone center) can be expressed as $\Gamma = A_{1g} + 2A_{2u} + 2B_{2g} + B_{1u} + 2E_{1u} + 2E_{2g} + E_{2u}$ (E modes are double degenerated), where the Raman-active modes are A_{1g}, E_{1g}, and E_{2g}, while the bulk B_{2g} modes are optically inactive. In the selected region of the Raman spectrum (17 nm flake) of Figure 1e can be identified the characteristic optical phonon modes A_{1g}, E^1_{2g} and the optically silent B^1_{2g} which begins to appear because of the lack of symmetry along the layer direction (not observable in the 37 nm flake). The E^1_{2g} mode involves the vibration of the Mo atoms in-plane with respect to the Te atoms, which vibrate in the opposite direction. This mode is usually used as the characterization peak for thermal transport measurements due to its clear and intense signal in comparison with the other modes,[38] while in the optical A_{1g} mode Mo vibrates out-of-plane and in in-phase directions. For the optothermal analysis, we will focus on the E^1_{2g} and the A_{1g} modes which are optically active in both samples.

Figure 2 shows the calibration of temperature coefficients for the supported and suspended parts of the E^1_{2g} and the A_{1g} modes while heating the substrate (temperature ranges from room temperature to 500 K). All of the measurements were collected after the sample's temperature was stable. The temperature increase leads to softening of the active Raman modes, and the E^1_{2g} and A_{1g} modes follow a systematic redshift with increasing temperature (see Figure 2a and b for suspended $MoTe_2$ sample 1). This evolution is given approximately by the linear equation $\Delta\omega = \chi_T \Delta T$ (Figure 2c

https://doi.org/10.1021/acsami.3c06134
ACS Appl. Mater. Interfaces 2023, 15, 35692−35700

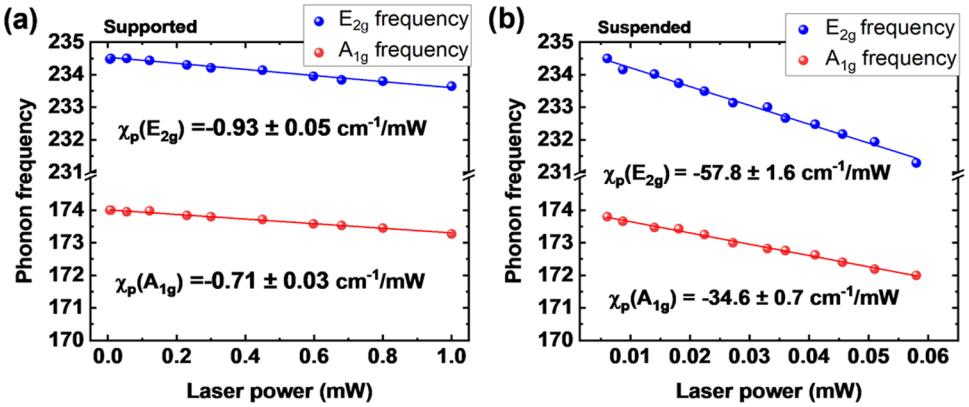

Figure 3. Power dependence of E^1_{2g} (blue circles) and A_{1g} (red circles) peak frequencies of (a) supported and (b) suspended $MoTe_2$ using 100× objective, including the respective χ_P values.

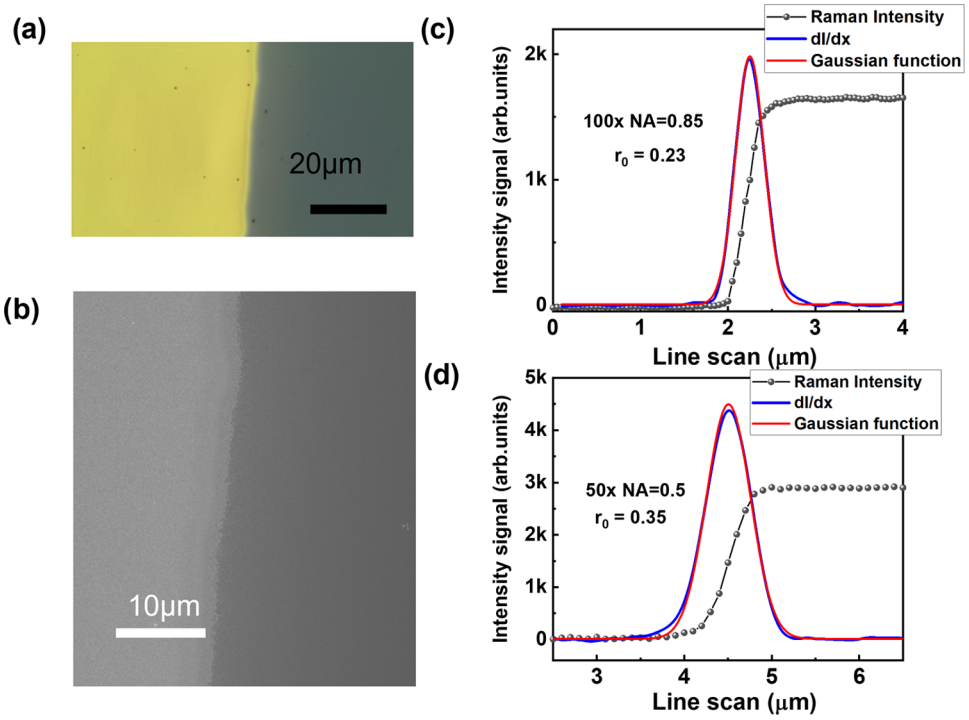

Figure 4. (a) Optical and (b) scanning electron microscope images of the Au edge. For the measurement of the beam spot profile, the cleaned Si substrate was coated with a layer of Au (about 300 nm thick) using an electron-beam evaporator. The dotted line corresponds to the scan line of the beam profile and indicates the extracted Raman intensity of the laser spot from (c) 100× objective (NA = 0.85) and (d) 50× (NA = 0.5).

and d), where χ_T is the first-order temperature coefficient for $MoTe_2$ optical modes and ΔT is the temperature change. Note that E^1_{2g}, the in-plane phonon mode, is more affected by the strain[42] and thermal expansion of the lattice with respect to the A_{1g}. Furthermore, the fitting χ_T parameters for suspended $MoTe_2$ are slightly different from the supported part because of the influence of the thermal expansion coefficient mismatch between the sample and the substrate.[43]

To extract the linear relation between the sample temperature and the absorbed laser power, we investigated the effect of laser-induced heat on the selected modes for $MoTe_2$ suspended and over Si substrate at various laser powers. All spectra were collected using 50× (numerical aperture, NA = 0.5) and 100× (NA = 0.85) objectives. To avoid sample heating and the appearance of nonlinear effects, the Raman characterization was done at lower power intensities within the linear dependence range (see Figure S1, Supporting Information). For example, in Figure 3, we can observe the power-dependence evolution of the mentioned modes for supported (Figure 3a) and suspended (Figure 3b) $MoTe_2$ sample 1 using 100× objective. The data has been extracted from the Lorentzian fit of the phonon modes as a function of the laser power. The power-dependence measurements for the $MoTe_2$ sample 2 and Raman shift evolution using a 50× objective can be found in Figures S4 and S5. In general, we have observed that in all of the cases, the Raman peaks downshift as the laser power increases, indicating a local heating of the sample. The redshift of E^1_{2g} and the A_{1g} modes is more evident for the suspended samples because the incident laser beam is the main contributor to the heat change of the sample.[32] The linear Raman shift rates can be expressed by the equation $\Delta\omega = \chi_P \Delta P$, where χ_P is the first-order power coefficient and ΔP is the change in the laser power.

https://doi.org/10.1021/acsami.3c06134
ACS Appl. Mater. Interfaces 2023, 15, 35692−35700

Table 1. Temperature and Power Coefficients, Thermal Conductivities, and Interfacial Thermal Conductances of $MoTe_2$

$MoTe_2$	mode	χ_T [cm^{-1}/K]	χ_P [cm^{-1}/mW] 100×	χ_P [cm^{-1}/mW] 50×	G [MW/m^2K]	k [W/m·K]
sample 1	A_{1g}	−0.0085 ± 0.0006	−34.6 ± 0.7	−21.4 ± 0.7		3.72 ± 0.26
suspended	E^1_{2g}	−0.0165 ± 0.0005	−57.8 ± 1.6	−32.3 ± 1.3		5.16 ± 0.24
sample 1	A_{1g}	−0.0075 ± 0.0004	−0.71 ± 0.03	−0.32 ± 0.02	~16.2[a]	~2.35[a]
supported	E^1_{2g}	−0.0138 ± 0.0003	−0.93 ± 0.05	−0.41 ± 0.01	~23.9[a]	~0.80[a]
sample 2	A_{1g}	−0.00977 ± 0.0004	−8.1 ± 0.6	−10.0 ± 0.6		13.2 ± 1.2
suspended	E^1_{2g}	−0.01519 ± 0.0007	−12.9 ± 1.2	−13.5 ± 0.9		12.8 ± 1.4
sample 2	A_{1g}	−0.0075 ± 0.0007	−1.05 ± 0.03	−0.67 ± 0.03	5.5 ± 1.7	18.1 ± 6.4
supported	E^1_{2g}	−0.01402 ± 0.0003	−1.35 ± 0.03	−0.83 ± 0.05	9.7 ± 2.3	22.0 ± 9.3

[a]The extracted values of the supported sample 1 require further experimental analysis with different substrates for better estimation of the errors. More information can be found in Figure S6.

By combining equations for χ_T and χ_P, we can obtain the change in temperature as a function of change in the absorbed laser power, defined as the thermal resistance R_m

$$R_m = \frac{\Delta T}{\alpha \Delta P} = \frac{\chi_P}{\alpha \chi_T} \tag{1}$$

where α is the absorption. We assume an absorption coefficient of 4.69×10^7 1/m for $MoTe_2$,[44] which gives α values of 0.55 and 0.82 for 17 and 37 nm $MoTe_2$ samples, respectively.

Thermal resistance given by eq 1 correlates the value of the temperature increase with increasing laser power. To link this value to the thermal conductivity of the material, we need to calculate the theoretically predicted temperature profile in the case of an external heat source applied to the material, which in our case is the illuminating laser beam. The heat is diffused in the plane of the $MoTe_2$, and the efficiency of the diffusion, and thus the overall temperature increase, is directly related to the thermal conductivity. Also, in the supported parts of the $MoTe_2$, the heat is transferred to the Si substrate, which acts as a heat sink. Neglecting the heat convection to air and assuming continuous heating by the laser beam, the steady-state temperature profile is determined by the heat diffusion equations[30]

$$\frac{k_1}{r}\frac{d}{dr}\left(r\frac{dT}{dr}\right) = -q_V(r), \text{ (suspended)} \tag{2}$$

$$\frac{k_2}{r}\frac{d}{dr}\left(r\frac{dT}{dr}\right) - \frac{G}{t}(T(r) - T_a) = -q_V(r), \text{ (supported)} \tag{3}$$

where $k_{1(2)}$ is the thermal conductivity of the suspended (supported) $MoTe_2$, G is the interfacial thermal conductance between the $MoTe_2$ and the substrate, t is the thickness of the $MoTe_2$ flake, T_a is the ambient temperature, and q_V is the volumetric optical heating from the Gaussian laser beam

$$q_V(r) = \frac{\alpha P}{\pi r_0^2 t}\exp\left(-\frac{r^2}{r_0^2}\right) \tag{4}$$

where r_0 is the laser beam radius. The laser beam radius was experimentally determined by performing line scan Raman spectroscopy across an Au layer-coated cleavage edge (Figure 4a,b) using 100× and 50× objectives. Then, the Si peak intensity was extracted as a function of the moving position (dI/dx), which can be fitted by a Gaussian function $\exp(-x^2/r_0^2)$ for both: 100× (Figure 4c) and 50× (Figure 4d). The experimental values of r_0 were 0.23 and 0.35 μm, which slightly differs from the estimated through numerical aperture 0.19 and 0.33 μm for 100× (NA = 0.85) and 50× (NA = 0.5), respectively. The temperature profile depends on whether the $MoTe_2$ layer is either suspended or supported, leading to different boundary conditions. In all cases, the applied boundary conditions are $dT/dr|_{r=0} = 0$, and $T(r \to \infty) = T(a)$, ensuring that the temperature stays finite at the origin and that the temperature is the ambient temperature far away from the laser-illuminated area.

We will first start our analysis on supported $MoTe_2$, for which eq 3 applies everywhere. This analysis will help us obtain k_2 and G, which are also needed to calculate the thermal conductivity for the suspended $MoTe_2$, k_1. By applying the aforementioned boundary conditions, we can solve the temperature profile by using the variation of parameters technique[30,45]

$$T(\gamma) = T_a + \frac{\alpha P}{\pi r_0^2 G}\left(K_0(\gamma)\int_0^{\gamma} I_0(y)\exp(-y^2/\gamma_0^2)y\,dy + I_0(\gamma)\int_{\gamma}^{\infty} K_0(y)\exp(-y^2/\gamma_0^2)y\,dy\right) \tag{5}$$

where we have defined an auxiliary parameter $\gamma(r) = r\sqrt{G/k_2 t}$ and $\gamma_0 = \gamma(r_0)$. The area of the illuminated laser beam determines the experimentally observed temperature T_m. This is obtained as an average temperature over the 2D space weighed by the Gaussian beam profile

$$T_m = \frac{\int_0^{\infty} T(r) q_V(r) r\,dr}{\int_0^{\infty} q_V(r) r\,dr} \tag{6}$$

and thus the observed temperature change is $\Delta T = T_m - T_a$, and by dividing this with absorbed laser power αP we have the analytical value for the thermal resistance R_m. Thus, by using eq 6 with 1, we have linked the experimentally obtained temperature increase with the analytical temperature profile determined by the thermal conductivity k_2 and interfacial thermal conductance G, which are the two unknown values. Thus, two different experiments are needed to determine them uniquely.

To determine k_2 and G, we follow the method presented by Cai et al.,[30] where the power-dependent Raman measurements are done for two different objectives, 100× and 50× in our case, which give two different thermal resistances R_m. By taking the ratio of these two values, we get a formula solely dependent on the ratio of the two parameters, k_2/G, which can then be solved numerically. Then, we applied the solved ratio to the thermal resistance of one of the objectives to extract both k_2

https://doi.org/10.1021/acsami.3c06134
ACS Appl. Mater. Interfaces 2023, 15, 35692−35700

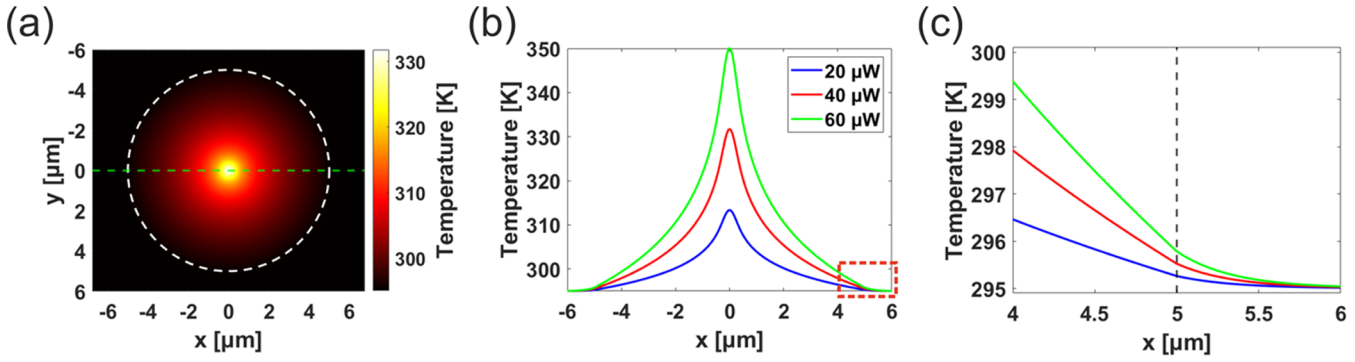

Figure 5. Temperature profile for suspended 37 nm $MoTe_2$ illuminated by a laser beam with 100× objective. (a) Heat map of the temperature profile for 40 μW laser power with a dashed white line indicating the edge of the hole. (b) Temperature profile along the x-axis indicated by the green dashed line in (a) for different laser powers. (c) Zoomed in at the edge around R = 5.0 μm.

and G. The results for the characterized modes of samples 1 and 2 are summarized in Table 1.

When the sample is suspended over the holes, eq 2 applies in the region $0 \le r < R$ and eq 3 in $r \ge R$, where R is the radius of the hole. In this case, two additional boundary conditions are needed, namely, that the temperature profile is continuous at R, and $-2\pi R k_{1,2} \mathrm{d}T/\mathrm{d}r|_{r=R} = \alpha P$, indicating that the heat transferred out of the suspended flake must equal the absorbed laser power.

By solving the differential equation, and assuming that $r_0 \ll R$, we get the temperature profile for suspended $MoTe_2$, namely, in the region $0 \le r < R$

$$T(r) = T_a + \frac{\alpha P}{2\pi R\sqrt{k_2 G t}} \frac{K_0\left(\sqrt{\frac{G}{k_2 t}} R\right)}{K_1\left(\sqrt{\frac{G}{k_2 t}} R\right)} + \frac{\alpha P}{2\pi k_1 t} \left[\ln\frac{R}{r} + \frac{1}{2} E_i\left(-\frac{r^2}{r_0^2}\right)\right] \quad (7)$$

where $E_i(-r^2/r_0^2)$ is the exponential integral.[46] The temperature profile in the region $r \ge R$ is given by eq (S1) in the Supplementary Information.

We can obtain the formula for k_1 by using eq 6 in 7, and then implementation of the power-dependent Raman measurement only for one objective would be sufficient, as there is only one unknown parameter. By carrying out the integration and then solving for k_1, we get the formula

$$k_1 = \frac{I}{\pi r_0^2 t}\left[R_m - \frac{1}{2\pi R\sqrt{k_2 G t}} \frac{K_0\left(\sqrt{\frac{G}{k_2 t}} R\right)}{K_1\left(\sqrt{\frac{G}{k_2 t}} R\right)}\right]^{-1} \quad (8)$$

where $I = \int_0^R \exp(-r^2/r_0^2)\left(\ln(R/r) + \frac{1}{2}E_i(-r^2/r_0^2)\right) r\mathrm{d}r$.

The simulated temperature profiles for suspended 37 nm $MoTe_2$ are given in Figure 5, with 100× objective. Figure 5a shows the temperature profile over the 2D plane for 40 μW laser power, with Figure 5b limiting itself to the x-axis, indicated by the green dashed line in Figure 5a. Figure 5c shows the zoomed-in part near the edges of the Si holes, where the material changes from suspended to supported, and the temperature decays to the room temperature T_a = 295 K. The decay length of the temperature on the supported part of 2D material is determined by the thermal conductivity of the material and the interfacial thermal conductance between the material and the substrate. Still, overall the temperature of the sample is close to the room temperature at the edges due to the large diameter of the holes compared with the spot size of the Gaussian beam and the Si substrate working as an effective heat sink. Thus, the exact values of k_2 and G do not significantly affect the calculated value of k_1, and the results are not substantially different if the substrate is assumed to be a perfect heat sink.[40] However, this assumption would not be valid in the case of much smaller holes or less heat-conducting substrate and better conducting 2D material.[30,33] Hence, we used the more comprehensive method by analyzing the supported part of the $MoTe_2$, which validates our results and gives more insight into the thermal dynamics of the material.

From the Raman measurements on the suspended 17 nm $MoTe_2$, we obtain $\chi_T = -0.0085 \pm 0.0006$ cm^{-1}/K and $\chi_P = -34.6 \pm 0.8$ cm^{-1}/mW for the A_{1g} mode and 100× objective, giving us thermal resistance $R_m = 7.3 \times 10^6$ K/W. Inserting this into eq 8, the thermal conductivity is extracted as $k_1 = 3.72 \pm 0.26$ W/m·K, which is substantially smaller when compared with other 2D materials. The reason might be high strain due to mechanical exfoliation, which can cause a significant decrease in thermal conductivity. Repeating the same analysis for 37 nm $MoTe_2$, we obtain $k_1 = 13.2 \pm 1.2$ W/m·K.

Table 1 summarizes the experimental results and the calculated thermal conductivities for supported and suspended $MoTe_2$ for both 17 nm and 37 nm samples. The extracted thermal conductivities $k_2 = 18.1 \pm 6.4$ W/m·K (supported) and $k_1 = 13.2 \pm 1.2$ W/m·K (suspended) for 37 nm $MoTe_2$ are considerably higher than the corresponding values for the 17 nm sample. This is in agreement with the results presented for MoS_2 by Yuan et al.,[47] where nonmonotonic thickness dependence of thermal conductivity was observed, and in particular, 17 nm thickness is expected to have lower thermal conductivity than relatively thicker samples due to more considerable surface scattering. The differences in thermal conductivity can also be attributed to the results of mechanical exfoliation, which are expected to vary from sample to sample. Furthermore, the interfacial thermal conductance between the $MoTe_2$ and Si substrate is lower for the 37 nm sample (G = 5.6 ± 1.7 MW/m^{2}K) than for the 17 nm sample (G = 16.2 MW/m^{2}K) in contrast to previous analysis performed on MoS_2.[33] This can be explained by the differences during the dry transfer process, as the thinner sample required an additional heating/cooling step resulting in a significantly improved contact

https://doi.org/10.1021/acsami.3c06134
ACS Appl. Mater. Interfaces 2023, 15, 35692−35700

between the substrate and the sample (see the Methods Section). Nevertheless, further analysis of the interfacial thermal conductance with different substrates and different $MoTe_2$ thicknesses are required. analysis.

CONCLUSIONS

In summary, we used the optothermal Raman method to experimentally determine the in-plane thermal conductivities and interfacial thermal conductance of $MoTe_2$ thin films with thicknesses 17 and 37 nm. The laser spot sizes were experimentally obtained by the knife edge method, which was slightly different than the theoretically predicted values and was proved to be essential to extract accurate thermal conductivity for the supported $MoTe_2$. The thermal conductivity of $MoTe_2$ was shown to be considerably lower than that of other TMD materials, with 17 nm $MoTe_2$ having remarkably low thermal conductivities $k_1 = 3.72 \pm 0.26$ W/m·K and $k_2 = 2.35$ W/m·K for the suspended and supported parts, respectively. Overall, we performed the first experimental study of the thermal properties in suspended $MoTe_2$ using the optothermal Raman technique. Our experimental results provide essential input on the fundamental thermal parameters and heat dissipation of $MoTe_2$ and confirm this material as a potential candidate for thermoelectric applications.

METHODS

Sample Fabrication. The characterized $MoTe_2$ flakes were first mechanically exfoliated from clean bulk crystals (HQ Graphene, 2H phase) using the polydimethylsiloxane (PDMS)-assisted dry transfer method.[48] The samples were transferred onto clean Si substrates with diameter holes of 9−10 μm and depth around 3 μm. The large diameter and depth of the fabricated holes ensure the elimination of possible artifacts from the influence of the substrate for the extraction of thermal conductivity. For the transfer, the positions of the Si holes and the $MoTe_2$ were aligned under an optical microscope (HQ Graphene, Manual transfer system HQ2D MAN). Once they were in contact, the Si substrate and PDMS were carefully separated by moving the substrate stage. The thinner sample 1 required an additional step where the sample was heated at 60 °C so that the PDMS was softened and the $MoTe_2$ adhesion to the PDMS was lost. However, the thermal expansion coefficient of both materials can lead to the formation of wrinkles which may affect the thermal conductivity and interfacial thermal conductance. To preserve the quality of the material, we kept the samples in a dry nitrogen box.

Fabrication of Si Holes. The silicon samples were cleaned using acetone, isopropanol, and O_2 plasma. The prepatterned holes of the Si substrates were fabricated before the deposition of the $MoTe_2$ as follows: (a) Photoresist AZ ECI 3027 was spin-coated on the samples at 3000 rpm and baked for 60 s at 100 °C. (b) The resist was exposed for 160 ms with Heidelberg μPG 501 maskless lithography system. (c) Samples were developed in 1 min 30 s in AZ-726 MIF developer. (d) After that, silicon was etched with reactive ion etching (RIE) for 8 min. (e) RIE was done with SF6 and O_2 plasma (300 W, 50 mTorr, and 6 sccm for O_2 and 7 sccm for SF6). (f) Lastly, the remaining resist was removed with a Microposit 1165 remover.

Raman Measurement. Raman spectra were collected using an inVia Qontor confocal Raman spectroscope (Renishaw) under 532 nm laser line excitation. The laser beam focused on the sample with 100× (NA = 0.85) and 50× (NA = 0.5) microscope objectives. All measurements were calibrated with silicon samples using the characteristic phonon peaks at 520.5 cm^{-1}. After measuring the phonon for calibration, we kept the spectrometer in the corresponding position in order to avoid displacements in the spectra; thus, our experimental values have an uncertainty smaller than 0.2 cm^{-1}. The samples were placed on a temperature-controlled heating platform to measure Raman peak shifts with temperature and laser power change (Linkam Stage THMS600). The samples were left to thermalize for 20 min at each temperature. To prevent additional laser heating, the temperature-dependent measurements were performed at low power intensity and close to the minimum value of the linear region presented in the power-dependent measurements for each sample (see Figures 3, S1, S4, and S5).

ASSOCIATED CONTENT

Data Availability Statement

The authors declare that the data supporting the findings of this study are available within the paper and in the Supporting Information files.

Supporting Information

The Supporting Information is available free of charge at https://pubs.acs.org/doi/10.1021/acsami.3c06134.

The online version contains supplementary material and includes nonlinear region of the absorbed power, laser irradiation in a few-layer $MoTe_2$, temperature- and power-dependent measurements for suspended and supported, estimation of the error of the thermal properties, the temperature profile of sample 1, and AFM of sample 1 (PDF)

AUTHOR INFORMATION

Corresponding Authors

Carlos Rodriguez-Fernandez − *Faculty of Engineering and Natural Sciences, Photonics, Tampere University, 33720 Tampere, Finland;* orcid.org/0000-0001-9024-9042; Email: carlos.rodriguezfernandez@tuni.fi

Humeyra Caglayan − *Faculty of Engineering and Natural Sciences, Photonics, Tampere University, 33720 Tampere, Finland;* orcid.org/0000-0002-0656-614X; Email: humeyra.caglayan@tuni.fi

Authors

Arttu Nieminen − *Faculty of Engineering and Natural Sciences, Photonics, Tampere University, 33720 Tampere, Finland;* orcid.org/0000-0001-5260-3215

Faisal Ahmed − *Department of Electronics and Nanoengineering, Aalto University, FI-00076 Aalto, Finland*

Jesse Pietila − *Faculty of Engineering and Natural Sciences, Photonics, Tampere University, 33720 Tampere, Finland;* orcid.org/0000-0003-3524-1114

Harri Lipsanen − *Department of Electronics and Nanoengineering, Aalto University, FI-00076 Aalto, Finland;* orcid.org/0000-0003-2487-4645

Complete contact information is available at: https://pubs.acs.org/10.1021/acsami.3c06134

Notes

The authors declare no competing financial interest.

ACKNOWLEDGMENTS

We acknowledge the financial support of the Academy of Finland Flagship Programme (PREIN) (320165, 320167). C.R.-F. acknowledges the European Union's Horizon 2020 research and innovation program under the Marie Skłodowska-Curie grant agreement No. 895369.

REFERENCES

(1) Roldán, R.; Silva-Guillén, J. A.; López-Sancho, M. P.; Guinea, F.; Cappelluti, E.; Ordejón, P. Electronic Properties of Single-layer and Multilayer Transition Metal Dichalcogenides MX2 (M = Mo, W and X = S, Se). *Ann. Phys.* **2014**, *526*, 347−357.

(2) Shen, T.; Penumatcha, A. V.; Appenzeller, J. Strain Engineering for Transition Metal Dichalcogenides Based Field Effect Transistors. *ACS Nano* **2016**, *10*, 4712−4718.
(3) Koperski, M.; Molas, M. R.; Arora, A.; Nogajewski, K.; Slobodeniuk, A. O.; Faugeras, C.; Potemski, M. Optical Properties of Atomically Thin Transition Metal Dichalcogenides: Observations and Puzzles. *Nanophotonics* **2017**, *6*, 1289−1308.
(4) Splendiani, A.; Sun, L.; Zhang, Y.; Li, T.; Kim, J.; Chim, C.-Y.; Galli, G.; Wang, F. Emerging Photoluminescence in Monolayer MoS2. *Nano Lett.* **2010**, *10*, 1271−1275.
(5) Wang, Q. H.; Kalantar-Zadeh, K.; Kis, A.; Coleman, J. N.; Strano, M. S. Electronics and Optoelectronics of Two-dimensional Transition Metal Dichalcogenides. *Nat. Nanotechnol.* **2012**, *7*, 699−712.
(6) Butler, S. Z.; Hollen, S. M.; Cao, L.; Cui, Y.; Gupta, J. A.; Gutiérrez, H. R.; Heinz, T. F.; Hong, S. S.; Huang, J.; Ismach, A. F.; Johnston-Halperin, E.; Kuno, M.; Plashnitsa, V. V.; Robinson, R. D.; Ruoff, R. S.; Salahuddin, S.; Shan, J.; Shi, L.; Spencer, M. G.; Terrones, M.; Windl, W.; Goldberger, J. E. Progress, Challenges, and Opportunities in Two-Dimensional Materials Beyond Graphene. *ACS Nano* **2013**, *7*, 2898−2926.
(7) Eda, G.; Maier, S. A. Two-Dimensional Crystals: Managing Light for Optoelectronics. *ACS Nano* **2013**, *7*, 5660−5665.
(8) Sun, Y.; Pan, J.; Zhang, Z.; Zhang, K.; Liang, J.; Wang, W.; Yuan, Z.; Hao, Y.; Wang, B.; Wang, J.; Wu, Y.; Zheng, J.; Jiao, L.; Zhou, S.; Liu, K.; Cheng, C.; Duan, W.; Xu, Y.; Yan, Q.; Liu, K. Elastic Properties and Fracture Behaviors of Biaxially Deformed, Polymorphic MoTe2. *Nano Lett.* **2019**, *19*, 761−769.
(9) Jariwala, D.; Sangwan, V. K.; Lauhon, L. J.; Marks, T. J.; Hersam, M. C. Emerging Device Applications for Semiconducting Two-Dimensional Transition Metal Dichalcogenides. *ACS Nano* **2014**, *8*, 1102−1120.
(10) Agarwal, V.; Chatterjee, K. Recent Advances in the field of Transition Metal Dichalcogenides for Biomedical Applications. *Nanoscale* **2018**, *10*, 16365−16397.
(11) Sun, Y.; Terrones, M.; Schaak, R. E. Colloidal Nanostructures of Transition-Metal Dichalcogenides. *Acc. Chem. Res.* **2021**, *54*, 1517−1527.
(12) Wu, J.; Liu, Y.; Liu, Y.; Cai, Y.; Zhao, Y.; Ng, H. K.; Watanabe, K.; Taniguchi, T.; Zhang, G.; Qiu, C.-W.; Chi, D.; Neto, A. H. C.; Thong, J. T. L.; Loh, K. P.; Hippalgaonkar, K. Large Enhancement of Thermoelectric Performance in MoS_2/h-BN Heterostructure due to Vacancy-induced Band Hybridization. *Proc. Natl. Acad. Sci. U. S. A.* **2020**, *117*, 13929−13936.
(13) Coleman, J. N.; Lotya, M.; O'Neill, A.; Bergin, S. D.; King, P. J.; Khan, U.; Young, K.; Gaucher, A.; De, S.; Smith, R. J.; Shvets, I. V.; Arora, S. K.; Stanton, G.; Kim, H.-Y.; Lee, K.; Kim, G. T.; Duesberg, G. S.; Hallam, T.; Boland, J. J.; Wang, J. J.; Donegan, J. F.; Grunlan, J. C.; Moriarty, G.; Shmeliov, A.; Nicholls, R. J.; Perkins, J. M.; Grieveson, E. M.; Theuwissen, K.; McComb, D. W.; Nellist, P. D.; Nicolosi, V. Two-Dimensional Nanosheets Produced by Liquid Exfoliation of Layered Materials. *Science* **2011**, *331*, 568−571.
(14) Snyder, G. J.; Snyder, A. H. Figure of Merit ZT of a Thermoelectric Device defined from Materials Properties. *Energy Environ. Sci.* **2017**, *10*, 2280−2283.
(15) Wickramaratne, D.; Zahid, F.; Lake, R. K. Electronic and Thermoelectric Properties of Few-layer Transition Metal Dichalcogenides. *J. Chem. Phys.* **2014**, *140*, No. 124710.
(16) Zhang, Z.; Xie, Y.; Ouyang, Y.; Chen, Y. A Systematic Investigation of Thermal Conductivities of Transition Metal Dichalcogenides. *Int. J. Heat Mass Transfer* **2017**, *108*, 417−422.
(17) Smith, R. J.; King, P. J.; Lotya, M.; Wirtz, C.; Khan, U.; De, S.; O'Neill, A.; Duesberg, G. S.; Grunlan, J. C.; Moriarty, G.; Chen, J.; Wang, J.; Minett, A. I.; Nicolosi, V.; Coleman, J. N. Large-Scale Exfoliation of Inorganic Layered Compounds in Aqueous Surfactant Solutions. *Adv. Mater.* **2011**, *23*, 3944−3948.
(18) Cho, S.; Kim, S.; Kim, J. H.; Zhao, J.; Seok, J.; Keum, D. H.; Baik, J.; Choe, D.-H.; Chang, K. J.; Suenaga, K.; Kim, S. W.; Lee, Y. H.; Yang, H. Phase Patterning for Ohmic Homojunction Contact in $MoTe_2$. *Science* **2015**, *349*, 625−628.
(19) Keum, D. H.; Cho, S.; Kim, J. H.; Choe, D.-H.; Sung, H.-J.; Kan, M.; Kang, H.; Hwang, J.-Y.; Kim, S. W.; Yang, H.; Chang, K. J.; Lee, Y. H. Bandgap Opening in Few-layered Monoclinic $MoTe_2$. *Nat. Phys.* **2015**, *11*, 482−U144.
(20) Kappera, R.; Voiry, D.; Yalcin, S. E.; Branch, B.; Gupta, G.; Mohite, A. D.; Chhowalla, M. Phase-engineered Low-resistance Contacts for Ultrathin MoS_2 Transistors. *Nat. Mater.* **2014**, *13*, 1128−1134.
(21) Duerloo, K.-A. N.; Li, Y.; Reed, E. J. Structural Phase Transitions in Two-dimensional Mo- and W-dichalcogenide Monolayers. *Nat. Commun.* **2014**, *5*, No. 4214.
(22) Kim, C.; Issarapanacheewin, S.; Moon, I.; Lee, K. Y.; Ra, C.; Lee, S.; Yang, Z.; Yoo, W. J. High-Electric-Field-Induced Phase Transition and Electrical Breakdown of MoTe2. *Adv. Electron. Mater.* **2020**, *6*, No. 1900964.
(23) Zakhidov, D.; Rehn, D. A.; Reed, E. J.; Salleo, A. Reversible Electrochemical Phase Change in Monolayer to Bulk-like MoTe2 by Ionic Liquid Gating. *ACS Nano* **2020**, *14*, 2894−2903.
(24) Wang, Y.; Xiao, J.; Zhu, H.; Li, Y.; Alsaid, Y.; Fong, K. Y.; Zhou, Y.; Wang, S.; Shi, W.; Wang, Y.; Zettl, A.; Reed, E. J.; Zhang, X. Structural Phase Transition in Monolayer MoTe2 Driven by Electrostatic Doping. *Nature* **2017**, *550*, 487.
(25) Ahmed, F.; Shafi, A. M.; Mackenzie, D. M. A.; Qureshi, M. A.; Fernandez, H. A.; Yoon, H. H.; Uddin, M. G.; Kuittinen, M.; Sun, Z.; Lipsanen, H. Multilayer MoTe2 Field-Effect Transistor at High Temperatures. *Adv. Mater. Interfaces* **2021**, *8*, No. 100950.
(26) Datye, I. M.; Rojo, M. M.; Yalon, E.; Deshmukh, S.; Mleczko, M. J.; Pop, E. Localized Heating and Switching in MoTe2-Based Resistive Memory Devices. *Nano Lett.* **2020**, *20*, 1461−1467. PMID: 31951419
(27) Yang, Z.; Zhang, D.; Cai, J.; Gong, C.; He, Q.; Xu, M.; Tong, H.; Miao, X. Joule Heating Induced Non-melting Phase Transition and Multi-level Conductance in MoTe2 Based Phase Change Memory. *Appl. Phys. Lett.* **2022**, *121*, No. 203508.
(28) Zulfiqar, M.; Zhao, Y.; Li, G.; Li, Z.; Ni, J. Intrinsic Thermal conductivities of monolayer Transition Metal Dichalcogenides MX2 (M= Mo, W; X= S, Se, Te). *Sci. Rep.* **2019**, *9*, No. 4571.
(29) Shafique, A.; Shin, Y.-H. Strain Engineering of Phonon Thermal Transport Properties in Monolayer 2H-MoTe2. *Phys. Chem. Chem. Phys.* **2017**, *19*, 32072−32078.
(30) Cai, W.; Moore, A. L.; Zhu, Y.; Li, X.; Chen, S.; Shi, L.; Ruoff, R. S. Thermal Transport in Suspended and Supported Monolayer Graphene Grown by Chemical Vapor Deposition. *Nano Lett.* **2010**, *10*, 1645−1651.
(31) Lee, J.-U.; Yoon, D.; Kim, H.; Lee, S. W.; Cheong, H. Thermal conductivity of suspended pristine graphene measured by Raman spectroscopy. *Phys. Rev. B* **2011**, *83*, No. 081419.
(32) Zhang, X.; Sun, D.; Li, Y.; Lee, G.-H.; Cui, X.; Chenet, D.; You, Y.; Heinz, T. F.; Hone, J. C. Measurement of Lateral and Interfacial Thermal Conductivity of Single- and Bilayer MoS2 and MoSe2 Using Refined Optothermal Raman Technique. *ACS Appl. Mater. Interfaces* **2015**, *7*, 25923−25929.
(33) Yan, R.; Simpson, J. R.; Bertolazzi, S.; Brivio, J.; Watson, M.; Wu, X.; Kis, A.; Luo, T.; Hight Walker, A. R.; Xing, H. G. Thermal Conductivity of Monolayer Molybdenum Disulfide Obtained from Temperature-Dependent Raman Spectroscopy. *ACS Nano* **2014**, *8*, 986−993.
(34) Peimyoo, N.; Shang, J.; Yang, W.; Wang, Y.; Cong, C.; Yu, T. Thermal conductivity determination of suspended mono-and bilayer WS_2 by Raman spectroscopy. *Nano Res.* **2015**, *8*, 1210−1221.
(35) Zhou, H.; Zhu, J.; Liu, Z.; Yan, Z.; Fan, X.; Lin, J.; Wang, G.; Yan, Q.; Yu, T.; Ajayan, P. M.; Tour, J. M. High Thermal Conductivity of Suspended Few-layer Hexagonal Boron Nitride Sheets. *Nano Res.* **2014**, *7*, 1232−1240.
(36) Cai, Q.; Scullion, D.; Gan, W.; Falin, A.; Zhang, S.; Watanabe, K.; Taniguchi, T.; Chen, Y.; Santos, E. J. G.; Li, L. H. High Thermal

https://doi.org/10.1021/acsami.3c06134
ACS Appl. Mater. Interfaces 2023, 15, 35692−35700

Conductivity of High-quality monolayer Boron Nitride and its Thermal Expansion. *Sci. Adv.* **2019**, *5*, No. eaav0129.
(37) Yin, S.; Zhang, W.; Tan, C.; Chen, L.; Chen, J.; Li, G.; Zhang, H.; Zhang, Y.; Wang, W.; Li, L. Thermal Conductivity of Few-Layer PtS_2 and $PtSe_2$ Obtained from Optothermal Raman Spectroscopy. *J. Phys. Chem. C* **2021**, *125*, 16129−16135.
(38) Easy, E.; Gao, Y.; Wang, Y.; Yan, D.; Goushehgir, S. M.; Yang, E.-H.; Xu, B.; Zhang, X. Experimental and Computational Investigation of Layer-Dependent Thermal Conductivities and Interfacial Thermal Conductance of One- to Three-Layer WSe_2. *ACS Appl. Mater. Interfaces* **2021**, *13*, 13063−13071.
(39) Renteria, J. D.; Ramirez, S.; Malekpour, H.; Alonso, B.; Centeno, A.; Zurutuza, A.; Cocemasov, A. I.; Nika, D. L.; Balandin, A. A. Strongly Anisotropic Thermal Conductivity of Free-Standing Reduced Graphene Oxide Films Annealed at High Temperature. *Adv. Funct. Mater.* **2015**, *25*, 4664−4672.
(40) Saleta Reig, D.; Varghese, S.; Farris, R.; Block, A.; Mehew, J. D.; Hellman, O.; Woźniak, P.; Sledzinska, M.; El Sachat, A.; Chávez-Ángel, E.; Valenzuela, S. O.; van Hulst, N. F.; Ordejón, P.; Zanolli, Z.; Sotomayor Torres, C. M.; Verstraete, M. J.; Tielrooij, K.-J. Unraveling Heat Transport and Dissipation in Suspended MoSe2 from Bulk to Monolayer. *Adv. Mater.* **2022**, *34*, No. 2108352.
(41) Shanks, H. R.; Maycock, P. D.; Sidles, P. H.; Danielson, G. C. Thermal Conductivity of Silicon from 300 to 1400 °K. *Phys. Rev.* **1963**, *130*, 1743−1748.
(42) Zhang, X.; Qiao, X.-F.; Shi, W.; Wu, J.-B.; Jiang, D.-S.; Tan, P.-H. Phonon and Raman scattering of Two-dimensional Transition Metal Dichalcogenides from Monolayer, Multilayer to bulk material. *Chem. Soc. Rev.* **2015**, *44*, 2757−2785.
(43) Lin, Z.; Liu, W.; Tian, S.; Zhu, K.; Huang, Y.; Yang, Y. Thermal Expansion Coefficient of Few-layer MoS2 Studied By Temperature-Dependent Raman spectroscopy. *Sci. Rep.* **2021**, *11*, No. 7037.
(44) Munkhbat, B.; Wróbel, P.; Antosiewicz, T. J.; Shegai, T. O. Optical Constants of Several Multilayer Transition Metal Dichalcogenides Measured by Spectroscopic Ellipsometry in the 300−1700 nm Range: High Index, Anisotropy, and Hyperbolicity. *ACS Photonics* **2022**, *9*, 2398−2407.
(45) Judek, J.; Gertych, A. P.; Świniarski, M.; Łapińska, A.; Dużyńska, A.; Zdrojek, M. High Accuracy Determination of the Thermal Properties of Supported 2D Materials. *Sci. Rep.* **2015**, *5*, No. 12422.
(46) Olver, F. W.; Lozier, D. W.; Boisvert, R. F.; Clark, C. W. *NIST Handbook of Mathematical Functions*; Cambridge University Press, 2010.
(47) Yuan, P.; Wang, R.; Wang, T.; Wang, X.; Xie, Y. Nonmonotonic Thickness-dependence of in-plane Thermal Conductivity of Few-layered MoS_2: 2.4 to 37.8 nm. *Phys. Chem. Chem. Phys.* **2018**, *20*, 25752−25761.
(48) Varghese, S.; Reig, D. S.; Mehew, J. D.; Block, A.; Sachat, A. E.; Chávez-Ángel, E.; Sledzinska, M.; Ballesteros, B.; Torres, C. M. S.; Tielrooij, K.-J. Fabrication and Characterization of Large-area Suspended MoSe2 Crystals Down to the Monolayer. *J. Phys.: Mater.* **2021**, *4*, No. 046001.

https://doi.org/10.1021/acsami.3c06134
ACS Appl. Mater. Interfaces 2023, 15, 35692−35700